

VASPKIT: A Pre- and Post-Processing Program for VASP code

V. Wang,^{1,*} N. Xu,² J.-C. Liu,³ G. Tang,⁴ and W. T. Geng⁵

¹*Department of Applied Physics, Xi'an University of Technology, Xi'an 710054, China*

²*College of Chemical and Biological Engineering, Zhejiang University, Hangzhou 310027, China*

³*Department of Chemistry and Key Laboratory of Organic Optoelectronics & Molecular Engineering of Ministry of Education, Tsinghua University, Beijing 100084, China*

⁴*Theoretical Materials Physics, Q-MAT, CESAM, Université de Liège, Liège, Belgium*

⁵*School of Materials Science & Engineering, University of Science and Technology Beijing, Beijing 100083, China*

(Dated: June 8, 2022)

The VASPKIT program aims to manipulate and analyze the input and output files from the widely-used VASP electronic structure package. It mainly includes two modules. The pre-processing module is designed to prepare and manipulate input files such as generation of necessary input files, symmetry analysis, arbitrary supercell transformation, suggested band paths generation for any crystal structure. The post-processing module is used to extract and analyze the raw output files obtained from the VASP package, including the calculated data about elastic mechanics, electronic structure, charge/spin density, electrostatic potential, optical and wave function in real space, etc. VASPKIT can be conveniently run in a menu mode or command line mode. This article gives an overview of the program structure and presents illustrative examples for some of its uses. Furthermore, it continues to be under development, with growing functionality, currently only supports VASP, however, it is easy to extend it to work directly with files from other electronic structure packages.

I. INTRODUCTION

Density functional theory (DFT) is one of the most used quantum chemical approaches to predict the structural, mechanical, electronic, mechanical and optical properties of materials. There are dozens of first-principles electronic-structure packages based on DFT have been developed so far, such as Abinit¹, VASP^{2,3}, Siesta⁴ or Quantum Espresso^{5,6}, which are capable of exploring remarkable material properties. One of the common features for these packages is which require post-processing to plot or extract into a human-readable format from the raw calculated data. Several popular post-processing packages, such as Python Materials Genomics (pymatgen)⁷ and Atomic Simulation Environment (ASE)⁸, provide efficient and powerful interfaces to extract, plot and analyze the calculated raw data efficiently but require the users to be proficient in Python programming language.

The purpose of VASPKIT is to provide a powerful and user friendly tool to perform initial setup for calculations and post-calculation analysis to derive various material properties from raw calculated data using VASP package.

II. PRE-PROCESSING MODULE

The workflow for the pre-processing module of VASPKIT package is illustrated in Fig. 1. First, the program reads POSCAR file and then prepare the rest three input files (INCAR, POTCAR and KPOINTS) for the VASP code. It is also can edit structure file such as building supercell, determine the symmetry by calling a crystal-symmetry search library - Spglib⁹, or generated the suggested band structure diagram paths based on the algo-

rithm proposed by Hinuma et al¹⁰.

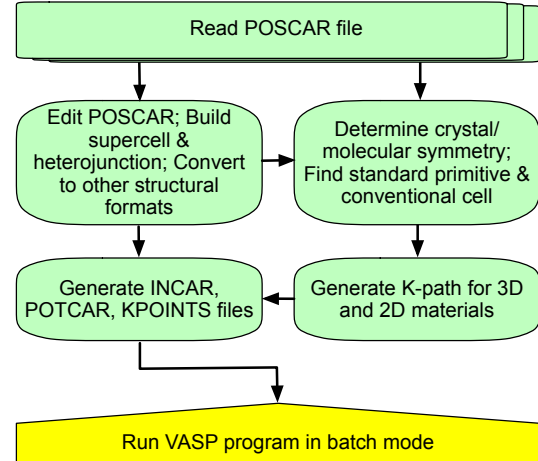


FIG. 1. (Color online) Flow chart describing the workflow for the pre-processing module implemented into the VASPKIT package.

A. Structure Manipulation

The crystal structures are often provided by basis vectors and point coordinates of labeled atoms. Lattice basis vectors \mathbf{A} are represented by three row vectors

$$\mathbf{A} = \begin{pmatrix} \mathbf{a} \\ \mathbf{b} \\ \mathbf{c} \end{pmatrix} = \begin{pmatrix} a_x & a_y & a_z \\ b_x & b_y & b_z \\ c_x & c_y & c_z \end{pmatrix} \quad (1)$$

The position of a ion is represented by a row vector

ether in fractional coordinates (x, y, z) with respect to basis vector lengths or in Cartesian coordinates (X, Y, Z)

$$\begin{pmatrix} X \\ Y \\ Z \end{pmatrix} = \mathbf{A}^T \begin{pmatrix} x \\ y \\ z \end{pmatrix} = \begin{pmatrix} a_x & b_x & c_x \\ a_y & b_y & c_y \\ a_z & b_z & c_z \end{pmatrix} \begin{pmatrix} x \\ y \\ z \end{pmatrix} \quad (2)$$

The convention of from a choice of lattice basis vector to another choice of basis vectors is related with transformation matrix M

$$\begin{pmatrix} \mathbf{a}' \\ \mathbf{b}' \\ \mathbf{c}' \end{pmatrix} = M \cdot \begin{pmatrix} \mathbf{a} \\ \mathbf{b} \\ \mathbf{c} \end{pmatrix} \quad (3)$$

VASPKIT can print the crystal symmetry (including symmetry operation, space group, etc), and find the conventional cell as well as the primitive cell for the underlying lattice, typically read from POSCAR file by employing the the symmetry analysis library Spglib.⁹ Furthermore, the package is currently has output interfaces to the electronic structure programs Quantum Espresso^{5,6}, Elk¹¹, Siesta⁴, as well as the XCrysDen¹², Crystallographic Information Framework (CIF), Protein Data Bank (PDB) formats.

III. POST-PROCESSING MODULE

Fig. 2 displays an overview of the post-processing features which have been implemented into the VASPKIT package.

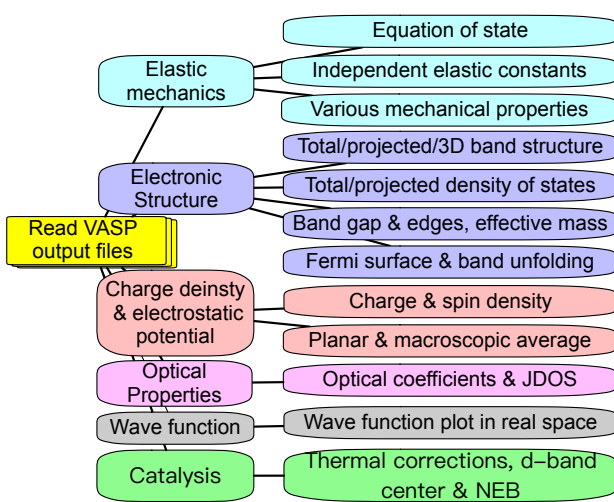


FIG. 2. (Color online) A structural overview of the post-processing module implemented into the VASPKIT package.

A. Elastic mechanics

The second-order elastic constants play a crucial role to understand the mechanical and dynamical properties of materials, especially provide information on the stability and stiffness of materials. Within the linear elastic region, the stress σ response of solids to external loading strain ε satisfies the generalized Hooke's law and can be simplified in the Voigt notation,¹³

$$\sigma_i = \sum_{j=1}^6 c_{ij} \varepsilon_j \quad (4)$$

where strain or stress are represented as a vector with 6 independent components respectively, i.e., $1 \leq i, j \leq 6$, and C_{ij} is the second order elastic stiffness tensor is expressed by a 6×6 symmetric matrix in units of GPa. The elastic stiffness tensor C_{ij} can be determined based on the first-order derivative of the stress-strain curves as expressed in Eq. 4, the so called stress-strain proposed by Nielsen and Martin.^{14,15} The number of independent elastic constants depends on the symmetry of crystals. The lower the symmetry, the more the independent elastic constants. For example, Cubic crystals have three but triclinic crystal utilitys have 21 independent elastic constants. The classification of the different crystal system with the corresponding number of independent elastic constants for bulk materials are summarized in Table I.^{16–18} An alternative approach to calculate theoretical elastic constants is based on the energy variation by applying small strains to the equilibrium lattice configuration.¹⁹ The elastic energy $\Delta E(V, \{\varepsilon_i\})$ of a solid under strain in the harmonic approximation is given by

$$\begin{aligned} \Delta E(V, \{\varepsilon_i\}) &= E(V, \{\varepsilon_i\}) - E(V_0, 0) \\ &= \frac{V_0}{2} \sum_{i,j=1}^6 C_{ij} \varepsilon_j \varepsilon_i, \end{aligned} \quad (5)$$

where $E(V, \{\varepsilon_i\})$ and $E(V_0, 0)$ are the total energies of the undistorted and distorted lattice cell, with the volume of V and V_0 , respectively. The energy-strain method corresponds that the elastic stiffness tensor is derived from the second-order derivative of the total energies versus strain.¹⁹ In general, the stress-strain method require higher computational precise to achieve the same accuracy as energy-strain method. Nevertheless, the former requires much smaller set of distortions than the latter.^{16,17,19–21} Considering that the energy-strain has less stress sensitivity than the stress-strain one, the former method has been implemented into the VASPKIT package. Furthermore, the determination of elastic stability criterion is also presented based on the necessary and sufficient elastic stability conditions in the harmonic approximation²² for various crystal systems proposed by Mouhat et al.^{16,17,23}

TABLE I. Classification of crystal systems, point group classes and space-group number are provided with the number of independent elastic constants for 3D materials.

Crystal system	Point group classes	Space-group numbers	No. of independent elastic constants
Triclinic	1, $\bar{1}$	1-2	21
Monoclinic	$m, 2, \frac{2}{2}$	3-15	13
Orthorhombic	$222, mm2, \frac{m}{m} \frac{2}{m} \frac{2}{m}$	16-74	9
Tetragonal I	$422, 4mm, \frac{4}{m} \frac{2}{m} \frac{2}{m}$	89-142	6
Tetragonal II	$4, \bar{4}, \frac{4}{m}$	75-88	7
Trigonal I	$32, 3m, \frac{3}{m} \frac{2}{m}$	149-167	6
Trigonal II	$3, \bar{3}$	143-148	7
Hexagonal	$622, 6mm, \bar{6}2m, \frac{6}{m} \frac{2}{m} \frac{2}{m}, 6, \bar{6}, \frac{6}{m}$	168-194	5
Cubic	$432, \bar{4}3m, \frac{4}{m} \frac{3}{m} \frac{2}{m}, 23, \frac{2}{m} \frac{3}{m}$	195-230	3

The flowchart of elastic utility as shown in Fig. 3. First, the package read the structural information (crystal lattice and atomic positions) from POSCAR file, and determine the corresponding space-group number; Second, the deformed structural and necessary input files are prepared; Next, the strain energies are calculated for each distorted structure by using VASP package; Then, a polynomial fitting procedure is applied to calculate the second derivative at equilibrium of the energy with respect to the strain; Finally, various mechanical properties such as bulk, shear, Young modulus and Poisson's ratio for polycrystalline materials are determined. Three of the most widely used averaging approaches have been implemented into the elastic utility: Voigt,¹³ Reuss²⁴ and Hill²⁵ schemes. Hill has shown that the Voigt and Reuss elastic moduli are the strict upper and lower bound, respectively.²⁵ The arithmetic mean of the Voigt and Reuss bounds termed the Voigt-Reuss-Hill (VRH) average is found as better approximation to the actual elastic behavior of a polycrystal material.

The relationship of lattice vectors between distorted and fully relaxed lattice cells is given by

$$\begin{pmatrix} \mathbf{a}' \\ \mathbf{b}' \\ \mathbf{c}' \end{pmatrix} = \begin{pmatrix} \mathbf{a} \\ \mathbf{b} \\ \mathbf{c} \end{pmatrix} \cdot (\mathbf{I} + \boldsymbol{\varepsilon}) \quad (6)$$

where \mathbf{I} is the identity matrix. The strain tensor $\boldsymbol{\varepsilon}$ is defined by

$$\boldsymbol{\varepsilon} = \begin{pmatrix} \varepsilon_1 & \frac{\varepsilon_6}{2} & \frac{\varepsilon_5}{2} \\ \frac{\varepsilon_6}{2} & \varepsilon_2 & \frac{\varepsilon_4}{2} \\ \frac{\varepsilon_5}{2} & \frac{\varepsilon_4}{2} & \varepsilon_3 \end{pmatrix} \quad (7)$$

where ε_i is the six components of the strain $\boldsymbol{\varepsilon}$.

B. Band Structure and Density of States

In order to plot a band structure, one need to define a set of k-points following a desired high-symmetry Bril-

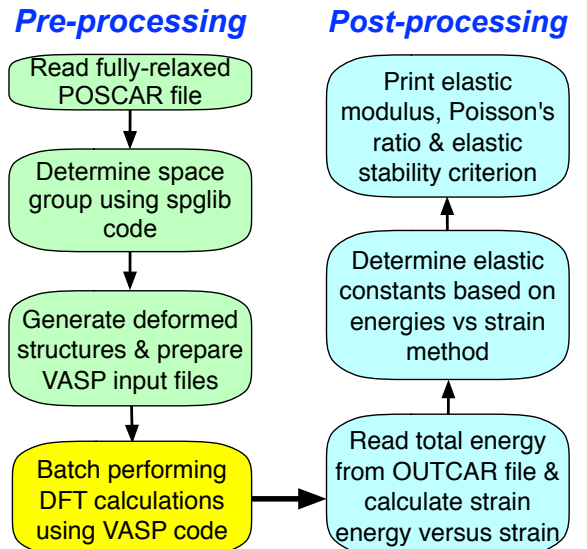


FIG. 3. (Color online) Flowchart of the algorithm to determine the second-order elastic constants based on energy-strain method used in the VASPKIT package.

louin zone directions. The VASPKIT k -path generation utility automatically generates a suggested k -path given the crystal structure based on the algorithms for bulk¹⁰ and two-dimensional materials²⁶. As an example, figure 4 shows the projected density of states and band structure of graphene.

C. Effective Masses of Carriers

Generally, when semiconductors with low carrier concentrations the band dispersions close to conduction or valence band extrema can be approximated as parabolic. Then the analytical expression of effective masses m^* for electrons and holes (in units of electron mass m_0) is given by

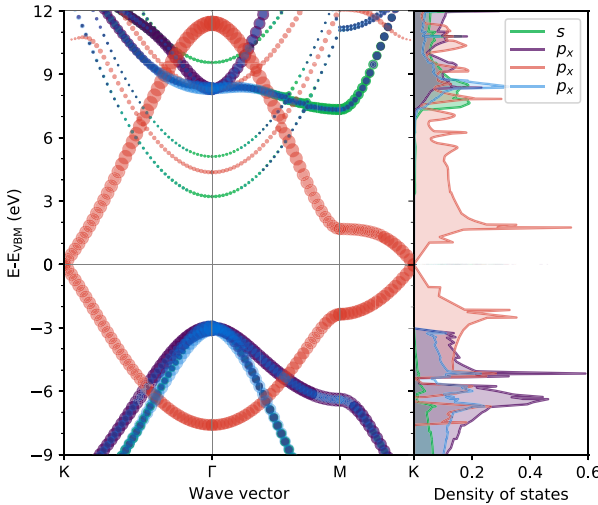


FIG. 4. (Color online) Projected band structure (left panel) and density of states (right panel) of graphene. The Fermi energy is set to zero.

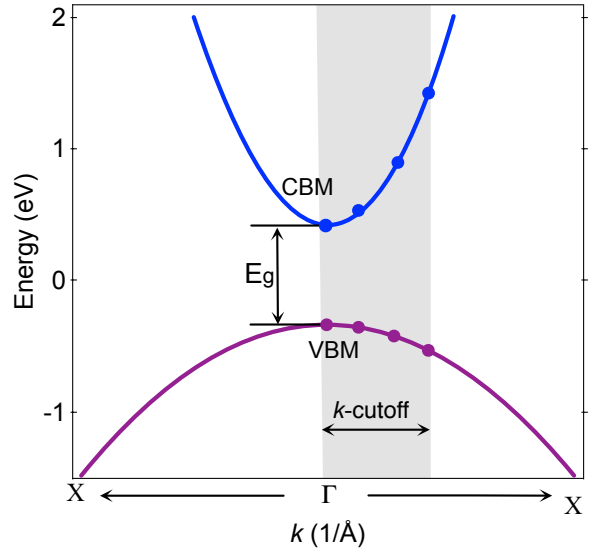


FIG. 5. (Color online) Schematic illustration of the determination of effective masses based on second-order polynomial fitting around the conduction and valence band extrema.

$$m^* = \hbar^2 \left[\frac{\partial^2 E(k)}{\partial^2 k} \right]^{-1} \quad (8)$$

where $E(k)$ are the energy dispersion relation functions described by band structures, and \hbar is the reduced Planck constant. Because m^* is inversely proportional to the curvature of the electronic dispersion in reciprocal space, suggesting that CB and VB edges with larger dispersions result in smaller effective masses. It is noteworthy that that the expression presented above should be not used in the some cases of the band dispersion relations show non-parabolic, for example, the linear dispersion in the band structure of graphene.²⁷

Figure 5 illustrates schematically the determination of effective masses by fitting the band dispersion relation using a second order polynomial. The effective masses of carriers are calculated on an ultrafine k -mesh of density uniformly distributed inside a circle of radius (k -cutoff). Haastrup *et al.* pointed that the inclusion of 3rd order terms stabilizes the fitting procedure and yields masses that are less sensitive to the details of the employed k -point grids.²⁸ Thus, a third order polynomial is also adopted to fit the band energy curvature in the VASPKIT package.

D. Charge Density and Potential Manipulation

For spin-polarized systems, the charge density $\rho(\mathbf{r})$ and magnetization (spin) density $m(\mathbf{r})$ are defined as

$$\begin{aligned} \rho(\mathbf{r}) &= \rho_{\uparrow}(\mathbf{r}) + \rho_{\downarrow}(\mathbf{r}) \\ m(\mathbf{r}) &= \rho_{\uparrow}(\mathbf{r}) - \rho_{\downarrow}(\mathbf{r}) \end{aligned} \quad (9)$$

where $\rho_{\uparrow}(\mathbf{r})$ and $\rho_{\downarrow}(\mathbf{r})$ are the spin-up and spin-down density. The spin density $\rho_{\sigma}(\mathbf{r})$ is expressed as

$$\rho_{\sigma}(\mathbf{r}) = \sum_{occ} \varphi_{i\sigma}^*(\mathbf{r}) \varphi_{i\sigma}(\mathbf{r}) \quad (10)$$

where σ and i are the spin- and band-index respectively. $\varphi_{i\sigma}(\mathbf{r})$ is the normalized single-particle wavefunction. occ means that be summed over all occupied states.

The charge density difference $\Delta\rho(\mathbf{r})$ can track the charge transfer to get an idea of such as what is interacting with what in the system and how strongly. The $\Delta\rho(\mathbf{r})$ can be obtained

$$\Delta\rho(\mathbf{r}) = \rho_{AB}(\mathbf{r}) - \rho_A(\mathbf{r}) - \rho_B(\mathbf{r}) \quad (11)$$

where $\rho_A(\mathbf{r})$, $\rho_B(\mathbf{r})$ and $\rho_{AB}(\mathbf{r})$ are the charge density of A and B reactants, and C product. VASPKIT package can extract charge-, spin-density, electrostatic potential as well as the difference of these quantities, and save as VESTA (.vasp)^{2,3,29}, XCrysDen (.xsf)¹², or Gaussian (.cube) formats³⁰.

From the three-dimensional electronic charge density and electrostatic potential one can get the average one-dimensional charge density $\bar{n}(z)$ and electrostatic potential $\bar{V}(z)$ by calculating the planar average function (\bar{f}):³¹

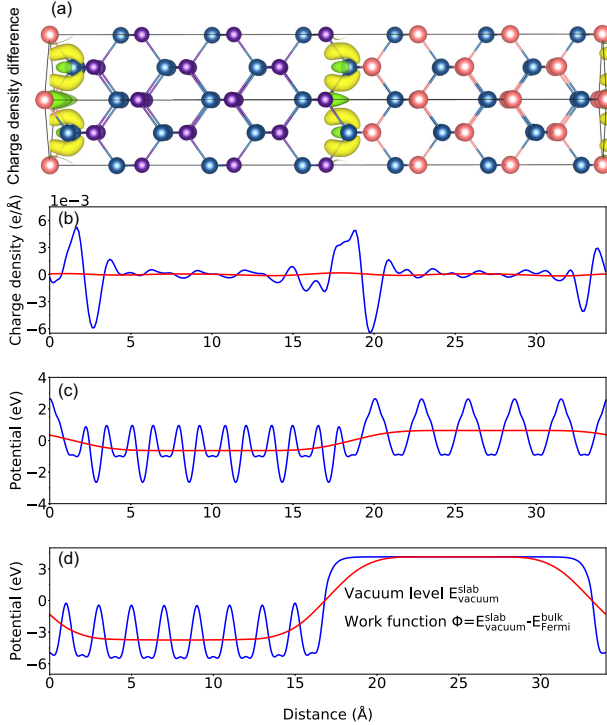


FIG. 6. (Color online) Calculated (a) charge density difference, planar- (blue line) and macroscopic averages (red line) of (b) charge density difference, (c) electrostatic potential of a GaAs/AlAs (100) heterojunction, and (d) electrostatic potential of a GaAs (110) slab. Ga atoms are shown in purple, As are blue, and Al are red.

$$\bar{f}(z) = \frac{1}{S} \int_S V(\mathbf{r}) dx dy \quad (12)$$

where S represents the area of a unit cell in the $x - y$ plane. Generally, this planar-averaged of charge density and potential exhibit periodic oscillations along the z axis due to the spatial distribution of the electrons and ionic cores. These oscillations are removed using a macroscopic averaging procedure:³¹

$$\bar{\bar{f}}(z) = \frac{1}{L} \int_{-L/2}^{L/2} \bar{f}(z) dz \quad (13)$$

where L is the length of the period of oscillation along z . By definition, this macroscopic average should produce a constant value in the bulk, and we observe that it indeed reaches a plateau value in the bulk-like regions of each layer in the superlattice. As an example, figure 6 shows the calculated planar and macroscopic averages of charge density difference and electrostatic potential for a (100)-oriented GaAs/AlAs heterojunction and a (110)-oriented GaAs slab. The vacuum level, work function, ionization energy, electron affinity, potential alignment,

which are parameters of great importance for any electronic material, can be determined as illustrated in Fig. 7.³²

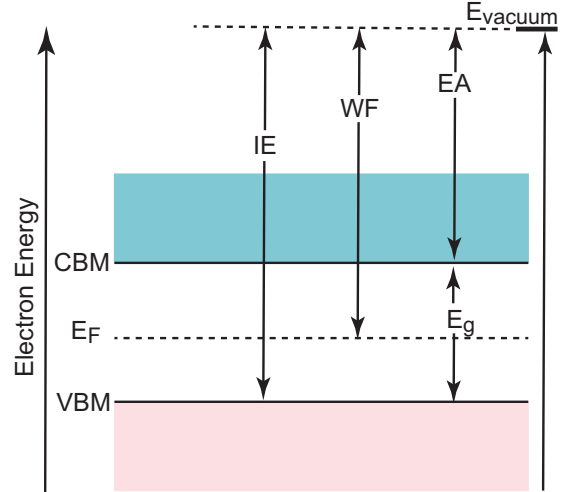


FIG. 7. (Color online) Calculated (a) charge density difference, planar- (blue line) and macroscopic averages (red line) of (b) charge density difference, (c) electrostatic potential of a GaAs/AlAs (100) heterojunction, and (d) electrostatic potential of a GaAs (100) slab.

E. Band Unfolding

The electronic structures of real materials are perturbed by various structural defects, impurities, fluctuations of the chemical composition in compound alloys and so on. In DFT calculations, these defects and incommensurate structures are usually investigated by using supercell (SC) models. However, interpretation of $E(\mathbf{k})$ versus \mathbf{k} band structures is most effective within the primitive cell (PC). Popescu and Zunger proposed the effective band structures (EBS) method which can unfold the band structures of supercells into the corresponding primitive cell BZ.^{33,34} Such band unfolding techniques greatly simplify the analysis of the results and enabling direct comparisons with experimental measurements, for example, angle-resolved photoemission spectroscopy (ARPES), often represented along the high-symmetry directions of the primitive cell BZ. The lattice vectors of the SC and PC satisfy $\mathbf{A} = M \cdot \mathbf{a}$, where \mathbf{A} and \mathbf{a} are the lattice vectors of SC and PC. The elements of transformation matrix M are integers ($m_{ij} \in \mathbb{Z}$) when build SC from PC. As a general convention, capital and lower case letters indicate quantities in the SC and PC respectively. A similar relation holds in reciprocal space:

$$\begin{pmatrix} \mathbf{B}_1 \\ \mathbf{B}_2 \\ \mathbf{B}_3 \end{pmatrix} = M^{-1} \cdot \begin{pmatrix} \mathbf{b}_1 \\ \mathbf{b}_2 \\ \mathbf{b}_3 \end{pmatrix} \quad (14)$$

The reciprocal lattice vectors \mathbf{g}_n (\mathbf{G}_n) in pbz (SBZ) expressed as

$$\begin{aligned}\mathbf{g}_n &= \sum_i n_i \mathbf{b}_i, \quad n_i \in \mathbb{Z} \\ \mathbf{G}_n &= \sum_i m_i \mathbf{B}_i, \quad m_i \in \mathbb{Z},\end{aligned}$$

where $\{\mathbf{g}_n\} \subset \{\mathbf{G}_n\}$, i.e. every lattice vector of the primitive cell Brillouin zone (pbz) is also one of the supercell Brillouin zone (SBZ).

For a given \mathbf{k} in pbz, there is a \mathbf{K} in the SBZ to which it folds into, and the two vectors are related by a reciprocal lattice vector \mathbf{G} in the SBZ:

$$\mathbf{k} = \mathbf{K} + \mathbf{G}_i, \quad i = 1, \dots, N_{\mathbf{K}}, \quad (15)$$

where $N_{\mathbf{K}} = \det M$ is the multiplicity of the supercell. When chose plane waves as basis functions, the individual weights of unfolded \mathbf{k} points are expressed as

$$\begin{aligned}P_{\mathbf{K}m}(k_j) &= \sum_{\mathbf{g}} |C_{\mathbf{K}m}(\mathbf{g} + \mathbf{k}_j - \mathbf{K})|^2 \\ &= \sum_{\mathbf{g}} |C_{\mathbf{K}m}(\mathbf{g} + \mathbf{G}_i)|^2\end{aligned}, \quad (16)$$

where $C_{\mathbf{K}m}$ is the plane wave coefficients of the eigenstate $|\mathbf{K}m\rangle$ and m is band index. The sum now runs over the reciprocal lattice vectors of the primitive cell \mathbf{g} . Clearly, all the filtered $C_{\mathbf{K}m}(\mathbf{g} + \mathbf{G}_j)$ coefficients only contribute to the spectral function.

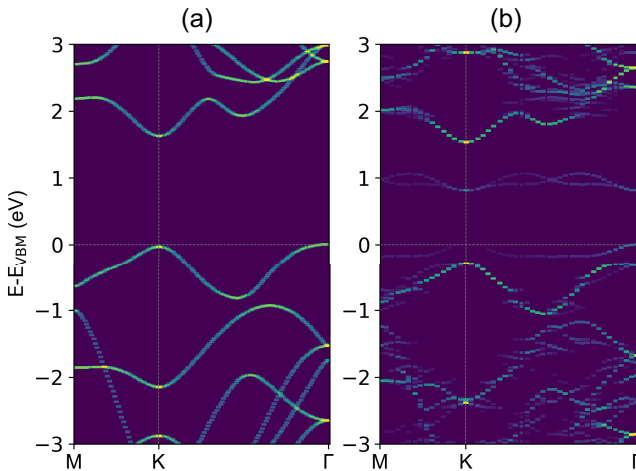


FIG. 8. (Color online) Calculated effective band structure of (a) Mo_9S_{18} and (b) $(\text{Mo}_9\text{S}_{17})$ 3×3 supercell unfolded into the primitive-cell Brillouin zone based on Eq. 16.

F. Linear Optical Properties

The linear optical properties can be obtained from the frequency-dependent complex dielectric function $\varepsilon(\omega)$

$$\varepsilon(\omega) = \varepsilon_1(\omega) + i\varepsilon_2(\omega) \quad (17)$$

where $\varepsilon_1(\omega)$ and $\varepsilon_2(\omega)$ are the real and imaginary parts of the dielectric function, and ω is the photon frequency. The frequency-dependent linear optical spectra, e.g., refractive index $n(\omega)$, extinction coefficient $\kappa(\omega)$, absorption coefficient $\alpha(\omega)$, energy-loss function (ω), and reflectivity $R(\omega)$ can be calculated from the real $\varepsilon_1(\omega)$ and the imaginary $\varepsilon_2(\omega)$ parts.³⁵

$$n(\omega) = \left[\frac{\sqrt{\varepsilon_1^2 + \varepsilon_2^2} + \varepsilon_1}{2} \right]^{\frac{1}{2}}, \quad (18)$$

$$k(\omega) = \left[\frac{\sqrt{\varepsilon_1^2 + \varepsilon_2^2} - \varepsilon_1}{2} \right]^{\frac{1}{2}}, \quad (19)$$

$$\alpha(\omega) = \sqrt{2}\omega \left[\frac{\sqrt{\varepsilon_1^2 + \varepsilon_2^2} - \varepsilon_1}{2} \right]^{\frac{1}{2}}, \quad (20)$$

$$L(\omega) = \text{Im} \left(\frac{-1}{\varepsilon(\omega)} \right) = \frac{\varepsilon_2}{\varepsilon_1^2 + \varepsilon_2^2}, \quad (21)$$

$$R(\omega) = \frac{(n-1)^2 + k^2}{(n+1)^2 + k^2}. \quad (22)$$

In Fig. 9 we present the linear optical spectra as determined by solving the Bethe-Salpeter Equation (BSE) on the top of G_0W_0 approximation. Since the GW approximation can correct the one electron eigenvalues obtained from DFT within a many-body quasiparticle framework, including the exchange and correlation effects in a self-energy term dependent on the one particle Green's function G and the dynamically screened Coulomb interaction W .^{36,37} Furthermore, the errors originating from the lack of ladder diagrams in determining W can be included through solution of the Bethe-Salpeter equation (BSE).³⁸ It would be expected that the GW-BSE calculated optical properties yield better agreement with experimental values. In the single-shot G_0W_0 approximation, the one-electron Green's function G is self-consistently updated within a single iteration, while the screened Coulomb interaction W is fixed at its initial value. It should be pointed that Eqs. 18 - 22 may not hold true for low-dimensional materials since the dielectric function is not straightforward and depends on the thickness of the vacuum layer when the low-dimensional

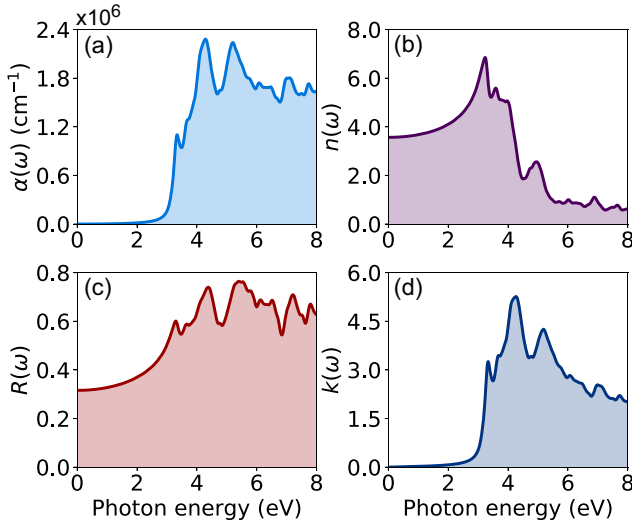


FIG. 9. (Color online) (a) absorption coefficient, (b) refractive index, (c) reflectivity and (d) extinction coefficient calculated using G_0W_0 -BSE approximation.

systems are simulated using a periodic stack of layers with sufficiently large interlayer distance L in the standard DFT calculations.^{39,40}

G. Joint Density of State

For a semiconductor, the optical absorption in direct band-to-band transitions is proportional to⁴¹

$$\frac{2\pi}{\hbar} \int_{BZ} |\langle v | \mathcal{H}' | c \rangle|^2 \frac{2}{(2\pi)^3} \delta(E_c(\mathbf{k}) - E_v(\mathbf{k}) - \hbar\omega) d^3k$$

where \mathcal{H}' is the perturbation associated with the light wave and $\langle v | \mathcal{H}' | c \rangle$ is the transition matrix from states in the valence band (VB) to states in the conduction band (CB); δ is the Dirac delta function which switches on this contribution when a transition occurs from one state to another, i.e., $E_c(\mathbf{k}) - E_v(\mathbf{k}) = \hbar\omega$. The factor 2 stems from the spin degeneracy. The integration is over the entire Brillouin zone (BZ). The matrix elements vary little within the BZ; Therefore, we can pull these out in front of the integral and obtain:

$$\frac{2\pi}{\Omega\hbar} |\langle v | \mathcal{H}' | c \rangle|^2 \cdot \int \frac{2\Omega}{(2\pi)^3} \delta(E_c(\mathbf{k}) - E_v(\mathbf{k}) - \hbar\omega) d^3k$$

where the factor $\Omega/(2\pi)^3$ normalizes the \mathbf{k} vector density within the Brillouin zone. The second term is the joint density of states (JDOS). After sum over all states within the first Brillouin zone and all possible transitions initiated by photons with a certain energy $\hbar\omega$ between valence and conduction bands, we obtain

$$\begin{aligned} n(\omega) &= \sum_{v,c} \frac{\Omega}{4\pi^3} \int d^3\mathbf{k} \delta(E_c(\mathbf{k}) - E_v(\mathbf{k}) - \hbar\omega) \\ &= 2 \sum_{v,c,\mathbf{k}} w_{\mathbf{k}} \delta(E_c(\mathbf{k}) - E_v(\mathbf{k}) - \hbar\omega), \end{aligned} \quad (23)$$

where Ω is the volume of the lattice cell, c and v belong respectively to the valence and conduction bands, $E(\mathbf{k})$ are the eigenvalues of the Hamiltonian, and $w_{\mathbf{k}}$ are weighting factors.

The Dirac Delta function in Eq. 23 can be numerically approximated by means of such as Gaussian function normalized to one:

$$G(\omega) = \frac{1}{\sigma\sqrt{2\pi}} e^{(E_{\mathbf{k},n'} - E_{\mathbf{k},n} - \hbar\omega)^2/2\sigma^2} \quad (24)$$

, where σ is the broadening parameter. To demonstrate this functionality, we show the calculated total and partial JDOS for $\text{CH}_3\text{NH}_3\text{PbI}$ and Si in Fig. 10. The total JDOS include all possible interband transitions from all the valence to all the conduction bands according to Eq. 23; while the partial JDOS consider only interband transitions from the highest valence band to the lowest conduction one.

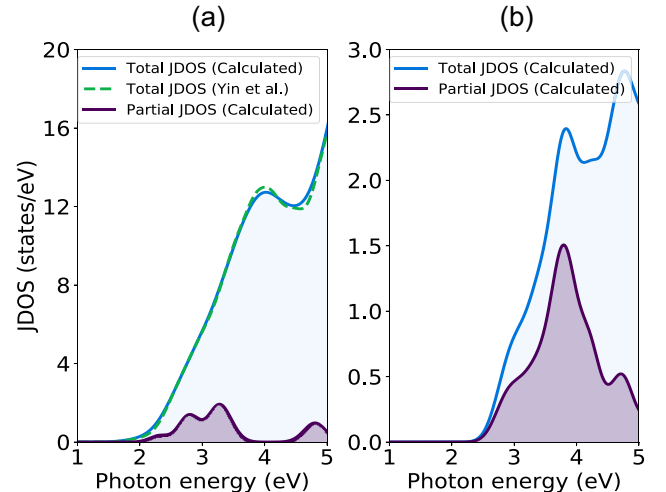


FIG. 10. (Color online) Calculated joint density of states for (a) $\text{CH}_3\text{NH}_3\text{PbI}$ and (b) Si. Blue and purple lines represent the total and partial joint density of states respectively. Adapted with permission from Ref. 42. Copyright 2014 WILEY-VCH Verlag GmbH & Co. KGaA.

H. Fermi surface

The physical properties of metals are determined by electrons occupying states near the Fermi energy, the knowledge of these states - especially the density of states

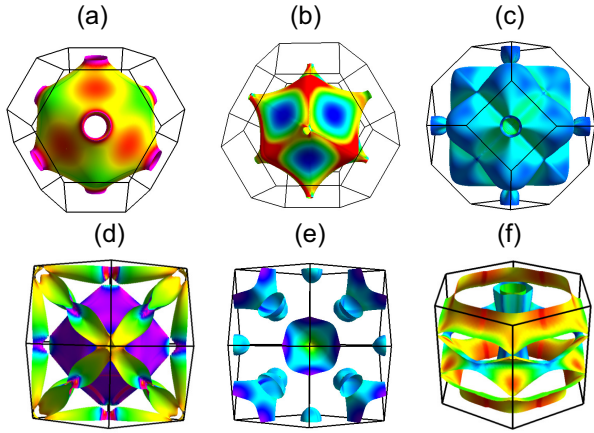


FIG. 11. (Color online) Calculated Fermi surface of (a) Cu, (b) spin up for Ni, (c) spin down for Ni, (d) spin up for Fe, (e) spin up down Fe and (f) MgB₂ respectively, visualized by FermiSurfer package⁴³.

at the Fermi energy and the characteristic features of the Fermi surface. Furthermore, the topology of Fermi surface is also related with superconductivity, electronic topological transitions, spin density wave, charge-density waves.⁴⁴ Several examples of Fermi surface are shown in Fig. 11.

I. Transition Dipole Moment

The transition dipole moment (TDM) or dipole transition matrix elements is the electric dipole moment associated with a transition between an initial state *a* and a final state *b*, denoted as P_{*a*→*b*},

$$P_{a \rightarrow b} = \langle \psi_a | \mathbf{r} | \psi_b \rangle = \frac{i\hbar}{(E_b - E_a) m} \langle \psi_a | \mathbf{p} | \psi_b \rangle \quad (25)$$

where ψ_a and ψ_b are energy eigenstates with energy E_a and E_b ; m is the mass of the electron. When chose plane waves as basis functions, the P_{*a*→*b*} is further expressed as

$$P_{a \rightarrow b} = \frac{i\hbar^2}{(E_b - E_a) m} \sum_i C_{ai} C_{bi} G_i \quad (26)$$

where C_{*a*}, C_{*b*} and G are plane-wave coefficients and reciprocal space vector with the same \mathbf{k} vector, respectively, summed over the the number of plane-waves. In general the TDM is a complex vector quantity that includes the phase factors associated with the two states. Its direction gives the polarization of the transition, which determines how the system will interact with an electromagnetic wave of a given polarization, while the sum of the squares of TDM, P^2 give the transition probabilities between to states.

In Fig. 12 we provide some specific examples to illustrate its use. It is seen that the calculated TDM amplitude is zero for transition between the conduction band minimum (CBM) and valence band maximum (VBM) at the Γ point, implying no optical absorption between these two states. On the other hand, the excellent optical absorption between CBM and VBM is predicted when all Ag is substituted by Bi atom.⁴⁵

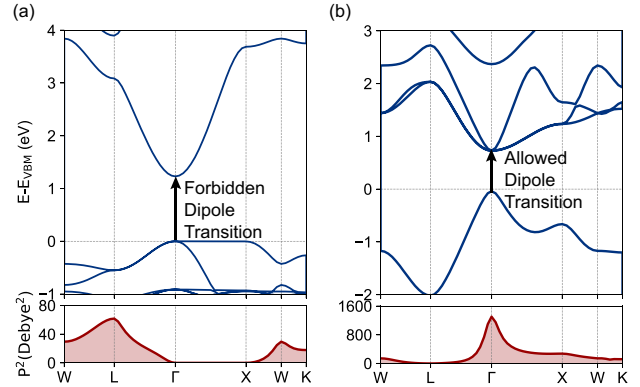


FIG. 12. (Color online) Calculated band structure (top panel) and transition dipole moment (bottom panel) for (a) Cs₂AgInCl₆ and (b) Cs₂InBiCl₆.

J. Wave Functions Visualization in Real Space

To visualize wave functions plots, the VASPKIT package first reads the pseudo wave function $\psi_{i,\mathbf{k}}(\mathbf{k})$ coefficients of the specified wave-vector \mathbf{k} point and band-index *i* and spin channel from the VASP WAVECAR file, and perform a fast Fourier transform algorithm to convert the $\psi_{i,\mathbf{k}}(\mathbf{k})$ from the reciprocal space to the real space [denoted as $\psi_{i,\mathbf{k}}(\mathbf{r})$]. Examples of calculated wave functions in real space are shown in Fig. 13.

IV. SUMMARY

We have presented a program for perform initial setup for calculations and post-calculation analysis to derive various material properties from raw calculated data using VASP code. We have demonstrated its capability through providing examples for each functionality through a set of four materials with unique characteristics.

ACKNOWLEDGMENTS

This work was supported in part by the National Natural Science Foundational of China under Grant 51877177 and in part by the Natural Science Basic Research Plan in

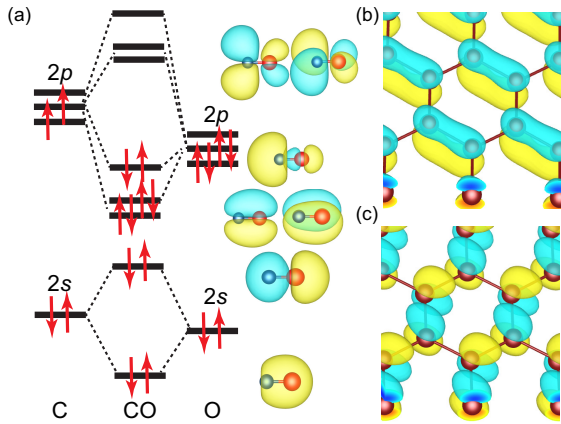


FIG. 13. (Color online) Calculated wave function in real space for (a) CO molecular, (b) VBM and (c) CBM of graphene.

Shaanxi Province under Grant 2019JM594. We acknowledge useful discussions with Xue-Fei Liu, Peng-Fei Liu, Zhao-Fu Zhang, Tian Wang, Dao-Xiong Wu and Qiang Li. We also thank various researchers around the world for reporting bugs and suggesting features, which have lead to significant improvements in the accuracy and robustness of the package.

* wangwei@icloud.com.

- ¹ X. Gonze, F. Jollet, F. A. Araujo, D. Adams, B. Amadon, T. Appelcourt, C. Audouze, J.-M. Beuken, J. Bieder, A. Bokhanchuk, E. Bousquet, F. Bruneval, D. Caliste, M. CÁZtA©, F. Dahm, F. D. Pieve, M. Delaveau, M. D. Gennaro, B. Dorado, C. Espejo, G. Geneste, L. Genovese, A. Gerossier, M. Giantomassi, Y. Gillet, D. Hamann, L. He, G. Jomard, J. L. Janssen, S. L. Roux, A. Levitt, A. Lherbier, F. Liu, I. Luka?evi?, A. Martin, C. Martins, M. Oliveira, S. PoncÁ©, Y. Pouillon, T. Rangel, G.-M. Rignanese, A. Romero, B. Rousseau, O. Rubel, A. Shukri, M. Stankovski, M. Torrent, M. V. Setten, B. V. Troeye, M. Verstraete, D. Waroquiers, J. Wiktor, B. Xu, A. Zhou, and J. Zwanziger, *Comput. Phys. Commun.* **205**, 106 (2016).
- ² G. Kresse and J. Furthmüller, *Comput. Mater. Sci.* **6**, 15 (1996).
- ³ G. Kresse and J. Furthmüller, *Phys. Rev. B* **54**, 11169 (1996).
- ⁴ J. M. Soler, E. Artacho, J. D. Gale, A. García, J. Junquera, P. Ordejón, and D. Sánchez-Portal, *J. Phys.: Condens. Matter* **14**, 2745 (2002).
- ⁵ P. Giannozzi, S. Baroni, N. Bonini, M. Calandra, R. Car, C. Cavazzoni, D. Ceresoli, G. L. Chiarotti, M. Cococcioni, I. Dabo, A. D. Corso, S. de Gironcoli, S. Fabris, G. Fratesi, R. Gebauer, U. Gerstmann, C. Gougaussis, A. Kokalj, M. Lazzeri, L. Martin-Samos, N. Marzari, F. Mauri, R. Mazzarello, S. Paolini, A. Pasquarello, L. Paulatto, C. Sbraccia, S. Scandolo, G. Sclauzero, A. P. Seitsonen, A. Smogunov, P. Umari, and R. M. Wentzcovitch, *J. Phys.: Condens. Matter* **21**, 395502 (2009).
- ⁶ P. Giannozzi, O. Andreussi, T. Brumme, O. Bunau, M. B. Nardelli, M. Calandra, R. Car, C. Cavazzoni, D. Ceresoli, M. Cococcioni, N. Colonna, I. Carnimeo, A. D. Corso, S. de Gironcoli, P. Delugas, R. A. DiStasio, A. Ferretti, A. Floris, G. Fratesi, G. Fugallo, R. Gebauer, U. Gerstmann, F. Giustino, T. Gorni, J. Jia, M. Kawamura, H.-Y. Ko, A. Kokalj, E. KÁCECÁEKbenli, M. Lazzeri, M. Marsili, N. Marzari, F. Mauri, N. L. Nguyen, H.-V. Nguyen, A. O. de-la Roza, L. Paulatto, S. Poncé, D. Rocca, R. Sabatini, B. Santra, M. Schlipf, A. P. Seitsonen, A. Smogunov, I. Timrov, T. Thonhauser, P. Umari, N. Vast, X. Wu, and S. Baroni, *J. Phys.: Condens. Matter* **29**, 465901 (2017).
- ⁷ S. P. Ong, W. D. Richards, A. Jain, G. Hautier, M. Kocher, S. Cholia, D. Gunter, V. L. Chevrier, K. A. Persson, and G. Ceder, *Comput. Phys. Sci.* **68**, 314 (2013).
- ⁸ A. H. Larsen, J. J. Mortensen, J. Blomqvist, I. E. Castelli, R. Christensen, M. Dułak, J. Friis, M. N. Groves, B. Hammer, C. Hargus, E. D. Hermes, P. C. Jennings, P. B. Jensen, J. Kermode, J. R. Kitchin, E. L. Kolsbørg, J. Kubal, K. Kaasbørg, S. Lysgaard, J. B. Maronsson, T. Maxson, T. Olsen, L. Pastewka, A. Peterson, C. Rostgaard, J. Schiøtz, O. SchÅ©tt, M. Strange, K. S. Thygesen, T. Vegge, L. Vilhelmsen, M. Walter, Z. Zeng, and K. W. Jacobsen, *J. Phys.: Condens. Matter* **29**, 273002 (2017).
- ⁹ A. Togo and I. Tanaka, arXiv preprint arXiv:1808.01590 (2018).
- ¹⁰ Y. Hinuma, G. Pizzi, Y. Kumagai, F. Oba, and I. Tanaka, *Comput. Phys. Sci.* **128**, 140 (2017).
- ¹¹ K. Dewhurst, S. Sharma, L. Nordstrom, F. Cricchio, F. Bultmark, H. Gross, C. Ambrosch-Draxl, C. Persson, C. Brouder, R. Armiento, *et al.*, ELK, <http://elk.sourceforge.net> (2016).
- ¹² A. Kokalj, *Comput. Mater. Sci.* **28**, 155 (2003).
- ¹³ W. Voigt *et al.*, *Lehrbuch der kristallphysik*, Vol. 962 (Teubner Leipzig, 1928).
- ¹⁴ O. H. Nielsen and R. M. Martin, *Phys. Rev. Lett.* **50**, 697 (1983).
- ¹⁵ O. Nielsen and R. M. Martin, *Physical Review B* **32**, 3792 (1985).
- ¹⁶ S. Zhang and R. Zhang, *Comput. Phys. Commun.* **220**, 403 (2017).
- ¹⁷ R. Golesorkhtabar, P. Pavone, J. Spitaler, P. Puschnig, and C. Draxl, *Comput. Phys. Commun.* **184**, 1861 (2013).
- ¹⁸ J. F. Nye *et al.*, *Physical properties of crystals: their representation by tensors and matrices* (Oxford university press, 1985).
- ¹⁹ Y. Le Page and P. Saxe, *Physical Review B* **63**, 174103 (2001).
- ²⁰ R. Yu, J. Zhu, and H. Ye, *Comput. Phys. Commun.* **181**, 671 (2010).

²¹ Y. Le Page and P. Saxe, *Phys. Rev. B* **65**, 104104 (2002).

²² Z. Hashin and S. Shtrikman, *J. Mech. Phys. Solids* **10**, 343 (1962).

²³ F. Mouhat and F. m. c.-X. Coudert, *Phys. Rev. B* **90**, 224104 (2014).

²⁴ A. Reuss and Z. Angnew, *Math Meth* **9**, 55 (1929).

²⁵ R. Hill, *Proc. Phys. Soc. London, Sect. A* **65**, 349 (1952).

²⁶ V. Wang, Y. Liang, Y. Kawazoe, and W. Geng, arXiv preprint arXiv:1806.04285 (2018).

²⁷ L. D. Whalley, J. M. Frost, B. J. Morgan, and A. Walsh, *Phys. Rev. B* **99**, 085207 (2019).

²⁸ S. Haastrup, M. Strange, M. Pandey, T. Deilmann, P. S. Schmidt, N. F. Hinsche, M. N. Gjerding, D. Torelli, P. M. Larsen, A. C. Riis-Jensen, J. Gath, K. W. Jacobsen, J. J. Mortensen, T. Olsen, and K. S. Thygesen, *2D Mater.* **5**, 042002 (2018).

²⁹ K. Momma and F. Izumi, *J. Appl. Crystallogr.* **44**, 1272 (2011).

³⁰ M. Frisch, G. Trucks, H. B. Schlegel, G. Scuseria, M. Robb, J. Cheeseman, G. Scalmani, V. Barone, B. Mennucci, G. Petersson, *et al.*, Inc., Wallingford, CT **200**, 28 (2009).

³¹ M. Peressi, N. Binggeli, and A. Baldereschi, *J. Phys. D: Appl. Phys.* **31**, 1273 (1998).

³² A. Kahn, *Mater. Horiz.* **3**, 7 (2016).

³³ V. Popescu and A. Zunger, *Phys. Rev. Lett.* **104**, 236403 (2010).

³⁴ V. Popescu and A. Zunger, *Phys. Rev. B* **85**, 085201 (2012).

³⁵ M. Fox, “Optical properties of solids,” (2002).

³⁶ L. Hedin, *Phys. Rev.* **139**, A796 (1965).

³⁷ F. Fuchs, J. Furthmüller, F. Bechstedt, M. Shishkin, and G. Kresse, *Phys. Rev. B* **76**, 115109 (2007).

³⁸ G. Onida, L. Reining, and A. Rubio, *Rev. Mod. Phys.* **74**, 601 (2002).

³⁹ F. Hüser, T. Olsen, and K. S. Thygesen, *Phys. Rev. B* **88**, 245309 (2013).

⁴⁰ P. Cudazzo, I. V. Tokatly, and A. Rubio, *Phys. Rev. B* **84**, 085406 (2011).

⁴¹ M. S. Dresselhaus, (2001).

⁴² W.-J. Yin, T. Shi, and Y. Yan, *Adv. Mater.* **26**, 4653 (2014).

⁴³ M. Kawamura, *Comput. Phys. Commun.* **239**, 197 (2019).

⁴⁴ S. B. Dugdale, *Phys. Scr.* **91**, 053009 (2016).

⁴⁵ W. Meng, X. Wang, Z. Xiao, J. Wang, D. B. Mitzi, and Y. Yan, *J. Phys. Chem. Lett.* **8**, 2999 (2017).